# Influence of OLA and FA ligands on the optical and electronic properties of $Cu_2ZnSn(S,Se)_4$ thin films and solar cells prepared from nanoparticle inks

S. Campbell[a,**], Y. Qu[a,**], L. Bowen[b], P. Chapon[c], V. Barrioz[a], N. S. Beattie[a], G. Zoppi[a,*]

[a] *Department of Mathematics, Physics and Electrical Engineering, Ellison Building, Northumbria University, Newcastle upon Tyne, NE1 8ST UK*
[b] *Department of Physics, Durham University, South Road, Durham DH1 3LE UK*
[c] *Horiba France SAS, Avenue de la Vauve, Passage Jobin Yvon CS45002, 91120 Palaiseau, France*

**Abstract**

The use of formamide (FA) as an alternative capping ligand to oleylamine (OLA) during the preparation of $Cu_2ZnSnS_4$ (CZTS) nanoparticle inks was investigated. Photoluminescence properties of the selenised CZTS absorber layers revealed quasi-donor acceptor pairs (QDAP) as the main transition for carrier recombination with similar electrostatic potential fluctuations in both type of ligands. In OLA layers the transition shifts from QDAP to band-impurity as temperature rises. Solar cell devices fabricated from FA $Cu_2ZnSn(Se,S)_4$ were shunted due to the high porosity of the film while in contrast, the combination of FA+OLA absorber yielded reduced back con-

*Corresponding author
**Contributed equally
*Email addresses:* s.campbell@northumbria.ac.uk (S. Campbell), y.qu@northumbria.ac.uk (Y. Qu), leon.bowen@durham.ac.uk (L. Bowen), patrick.chapon@horiba.com (P. Chapon), vincent.barrioz@northumbria.ac.uk (V. Barrioz), neil.beattie@northumbria.ac.uk (N. S. Beattie), guillaume.zoppi@northumbria.ac.uk (G. Zoppi)

tact barrier height, lower series resistance and higher fill factor and efficiency compared to OLA devices. This is a direct result of the removal of the fine grain carbon rich layer from the back contact interface usually present in films prepared with OLA only.

*Keywords:* $Cu_2ZnSn(S,Se)_4$, Thin film solar cells, Photoluminescence (PL), Formamide

---

## 1. Introduction

As a promising thin film photovoltaic material, kesterite $Cu_2ZnSn(S,Se)_4$ (CZTSSe) has attracted continual research interest for a marketable and industrial relevant photovoltaic technology. The current record of 12.6% has been obtained with a solution approach using reactive hydrazine as the solvent (Wang et al., 2014). In a less hazardous environment, $Cu_2ZnSnS_4$ (CZTS) nanoparticle inks annealed in the presence of Se has resulted in a device with efficiency as high as 9.3% (Hages et al., 2016). However, one of the current limitations of this method is the presence of a fine grain (FG) layer between the CZTSSe large grain (LG) layer and the back contact which is likely to reduce device performance via carrier recombination through traps, interface states and increased grain boundary density. This FG layer is a direct result of the use of a long carbon chain ligand, oleylamine (OLA), for the nanoparticle inks synthesis step. Alternative nanoparticle ink-based approaches have also been suggested (Wang et al., 2016).

Huang et al. recently suggested the use of formamide (FA) instead of OLA to produce single CZTS absorber layer without the FG layer (Huang et al., 2015). Surprisingly, despite a complete comparison of the microstructure properties of the absorber layer (Huang et al., 2016), there is no functional device reported from nanoparticle synthesized with FA. In this paper, we demonstrate working solar cells using a dual ligands approach via a stack of FA and OLA based absorbers: the FA absorber is used to provide a reduced back contact barrier height while the OLA absorber ensures a functioning *pn*-junction. Furthermore, the detailed luminescence properties of the two types of absorber and device parameters of working solar cells using dual

ligands are presented.

## 2. Theory

$V_{oc}$ deficit remains the major obstacle to achieving higher efficiency in kesterite solar cells. The presence of a random distribution of unscreened charged defects which creates electrostatic potential fluctuations of the valence and conduction bands has been suggested as a cause of severe $V_{oc}$ deficit in kesterite devices (Gokmen et al., 2013; Bourdais et al., 2016; Courel et al., 2017). These charged defects can be either acceptors or donors but in the case of highly compensated semiconductors such as CZTSSe, both types are present. Electrostatic potential fluctuations are characterised as a constant bandgap with parallel shifts in the valence and conduction band energies as shown in Fig.1. The presence of such fluctuations in the energy bands of a semiconductor results in absorption tails located at the bandgap edges. The exponentially decaying band tail states with energy less than the semiconductor energy bandgap $E_g$ results in a broad asymmetric photoluminescence (PL) spectrum (Levanyuk and Osipov, 1981; Shklovskij and Efros, 1984). Such behaviour can also be explained by the presence of bandgap fluctuations caused by microscopic variations in the stoichiometry of the kesterite material and/or the presence of secondary phases (Scragg et al., 2015).

Evidence of the presence of an electrostatic potential fluctuation is the significant red-shift of the energy of the maximum of the PL peak ($E_{PL}$) compared to the bandgap of the material. In materials suffering from this problem, the electrostatic potential fluctuation ($\gamma$) can be estimated by (Dirnstorfer et al., 1998):

$$\gamma^5 = \left(\frac{e^2}{4\pi\epsilon_0\epsilon_r}\right)^4 \frac{N_t^2\hbar^2}{m_r m_0} \tag{1}$$

where $m_r$ is the reduced effective mass given by $m_r = (m_e m_h)/(m_e + m_h)$, $m_e$ is the effective electron mass, $m_h$ is the effective hole mass, $m_0$ is the electron mass, $\hbar$ is the reduced Planck's constant, $\epsilon_0$ is permittivity of vacuum, $\epsilon_r$ is relative permittivity (or dielectric constant) and $N_t$ is the total charged defect density (both radiative and non-radiative).

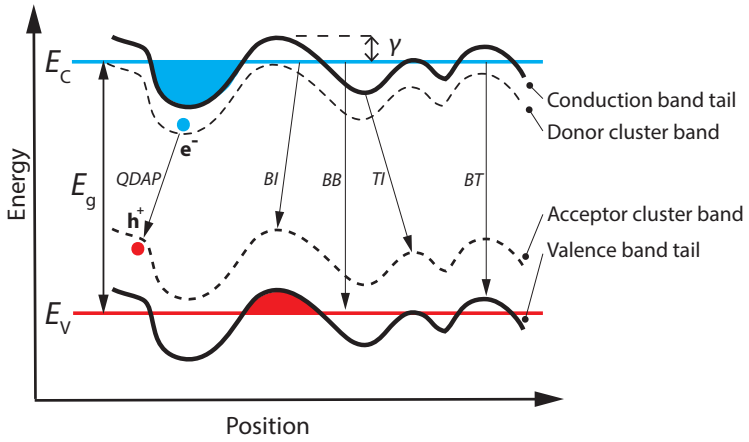


Figure 1: Schematics of electrostatic potential fluctuation where a strong perturbation of the energy bands is caused by a high density of localised charged defects resulting in deeper band-tail states (the solid colour shows a potential well region). Possible radiative transitions are shown: quasi donor acceptor pair (QDAP), band-impurity (BI), band-band (BB), tail-impurity (TI) and band-tail (BT).

The spectral shape of emission lines from a semiconductor with fluctuating potential of the energy bands is determined by the density of states (DOS) of charge carriers. A model has been proposed where the absorption

tails due to an electrostatic potential fluctuation are treated like defects. The low energy tail of emissions *I(E)* can therefore be described by (Siebentritt et al., 2006):

$$I(E) \sim exp\left(-\frac{(E-E_0)}{2\gamma^2}\right)^2 \tag{2}$$

where $E_0$ is the average emission energy in the case of fluctuating potentials (Siebentritt et al., 2006). The values of $\gamma$, and therefore $N_t$, can be deduced from the defect-model Gaussian fit.

There are two main models for understanding the dominant recombination mechanism involving sub-bandgap defect states in CZTSSe: (i) electrostatic potential fluctuation as previously detailed and (ii) quasi donor acceptor pair (QDAP) model (Yu, 1977; Schumacher et al., 2006) and both are fundamentally linked. The QDAP model describes the distribution of radiative donor/acceptor states (which are a proportion of $N_t$) that contribute to this potential fluctuation. The spectral position of the QDAP PL maximum $E_{PL}$ can be described as (Schumacher et al., 2006)

$$E_{PL} = E_g - (E_D + E_A) + \frac{e^2}{4\pi\epsilon_0\epsilon_r s} \tag{3}$$

where $E_D$ and $E_A$ are the donor and acceptor energy levels separated from the conduction band minimum (CBM) and valence band maximum (VBM), respectively and $s$ is the separation distance between donor and acceptor.

The last term in Eq.(3) describes the Coulomb potential which exists due to the attraction of the donor- and acceptor-like defects. A blue-shift in $E_{PL}$ is observed with increasing excitation intensity. More donor and acceptor states

become populated with escalating intensity, reducing the separation between these charge clusters and increasing their Coulomb interaction. This induces a shift of the emission peak towards higher energy and is a charcteristic of QDAP recombination observed in excitation-dependent PL spectra (Yu, 1977).

Previous reports (Gershon et al., 2013; Tai et al., 2015) have estimated the QDAP density using Eq.(3) by making the following assumptions (i) at low laser intensity, the spatial separation of charged defects is large enough such that there is no Coulombic interaction between the charged acceptor and donor clusters and (ii) there is maximum Coulombic attraction when all QDAP states are occupied which occurs when the QDAP peak saturates. Thus, the average separation distance $s$ between donor and acceptor can be estimated by equating the magnitude of blue-shift to Coulombic interaction term in Eq. (3). Consequently, the QDAP density $N_D$ can be estimated by assuming (Shklovskij and Efros, 1984)

$$s = \left(\frac{4\pi N_D}{3}\right)^{-\frac{1}{3}} \tag{4}$$

## 3. Materials and methods

### *3.1. Ink synthesis, precursor deposition and CZTSSe growth*

CZTS nanoparticles in this study were produced by injection of metallic precursors and sulphur into a hot solvent (more details about the nanoparticle synthesis are given in supplementary material). Oleylamine (OLA) with long hydrocarbon chain was firstly chosen as the capping ligand to prevent

the agglomeration of nanoparticles during fabrication (CZTS nanoparticles referred to as CZTS OLA) (Qu et al., 2014). Alternatively, formamide (FA) was chosen as the solvent in the synthesis of CZTS nanoparticles (referred to as CZTS FA) (Huang et al., 2015). The resulting nanoparticle inks are then spin coated on Mo-glass substrates to make CZTS thin films (Qu et al., 2016*a*). The thin films comprising CZTS nanoparticles were selenised in a tube furnace in order to promote grain growth, resulting in CZTSSe absorbers. Selenium pellets were placed directly under the substrate of the as-deposited precursor thin films encapsulated in a graphite box. The furnace was evacuated (6.0 x $10^{-3}$ mbar) and an argon atmosphere ($\sim$ 10 mbar) was provided before the temperature was increased ($\sim$ 20 °C /min) to 500 °C. This temperature was then held for 20 minutes before being cooled down rapidly ($\sim$ 20°C /min) as detailed elsewhere (Qu et al., 2016*b*).

### *3.2. Device fabrication*

Solar cells were fabricated from the CZTSSe thin films by the sequential deposition of CdS/intrinsic ZnO (*i*-ZnO)/indium tin oxide (ITO)/Ni-Al layers on top of the Mo/CZTSSe absorber. Chemical bath deposition was used to form a $\sim$ 55 nm CdS buffer layer followed by magnetron sputtering of the transparent oxide layers ($\sim$ 35 nm of *i*-ZnO and $\sim$ 200 nm of ITO). The devices were completed by deposition of the front contact grid via electron beam evaporation of Ni ($\sim$ 50 nm) and Al ($\sim$ 1 $\mu$m) through a shadow mask. Nine 0.16 $cm^2$ cells were defined by mechanical inscription.

### *3.3. Characterisation*

The structure of the CZTSSe thin films from different CZTS was exam-

ined using X-ray diffraction (XRD) carried out with a Siemens diffractometer using a Cu K$\alpha$ radiation source. Raman spectroscopy was performed with a Horiba microscope using a 632.8 nm HeNe ion laser. The thin film morphology was determined using a Tescan scanning electron microscope (SEM) attached with Oxford Instruments energy dispersive X-ray spectroscopy (EDS) kit. The solar cell efficiency was measured using an Abet Technologies solar simulator at 1-sun (100 mW/cm$^2$) illumination with a simulated air mass 1.5Global spectrum. The PL spectra were measured using a Horiba Jobin Yvon fully automated spectrometer fitted with an InGaAs PMT detector cooled to -30°C to reduce noise. A 532 nm continuous wave diode-pumped solid state (CW-DPSS) laser was used as an excitation source. All PL measurements were performed on selenised absorber layers deposited on Mo coated glass. Further details of the experimental PL setup can be found in the supplementary information section. Elemental depth profiling was performed by glow-discharge optical emission spectroscopy (GDOES, Horiba GD-profiler 2) using an Ar plasma with a crater size of 4 mm in diameter.

## 4. Results and Discussion

### *4.1. Material properties*

XRD was first used to confirm and compare the crystal structure of the selenised films. In addition to the peaks belonging to Mo and $MoSe_2$, both spectra reveal distinct peaks of (112), (220), (312) planes that can be assigned to kesterite CZTSe (PDF 052-0868) as shown in Fig.2a. However, these characteristic peaks are slightly shifted to higher angles as residual sulphur is present in the lattice (from EDS data Supp.Table 1). Due to the increased

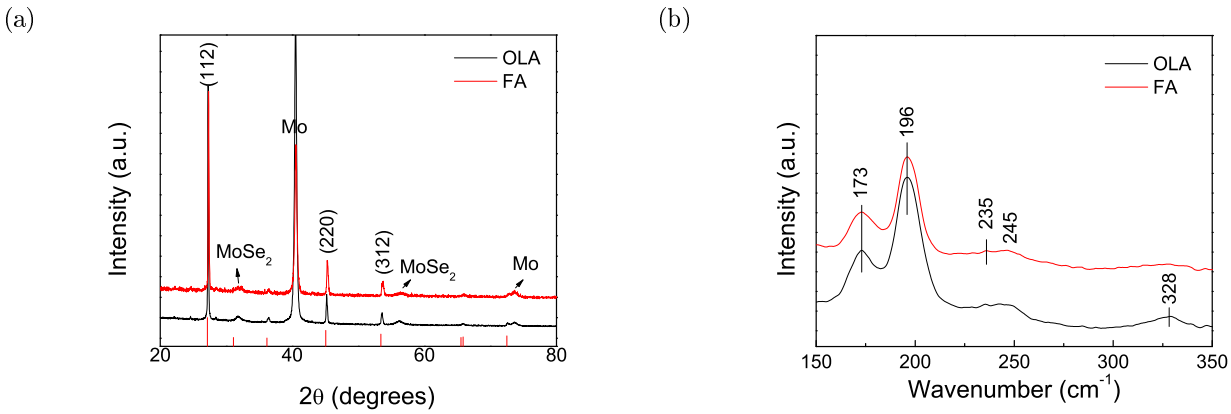


Figure 2: (a) XRD patterns and (b) Raman spectra of selenised CZTSSe absorber made from CZTS OLA and CZTS FA nanoparticles. The distinct XRD peaks in (a) matchl with the reference pattern of CZTSe (PDF 052-0868) given at the bottom.

Cu/(Zn + Sn) and decreased Zn/Sn ratio, a zinc loss process was observed after selenisation for both samples. In addition, a difference in the selenium and sulphur exchange process (i.e. Se/(Se+S) ratio) is observed between the two samples. For the CZTSSe OLA sample, 89% of sulphur is replaced by selenium and this increases to 98% for the CZTSSe FA sample. Compared with the dense CZTS OLA precursor film, the porous structure of the CZTS FA sample (see Supp.Fig.1) is likely to facilitate more selenium diffusion and incorporation into the thin films.

The crystal quality of both samples was further studied by Raman spectroscopy to rule out possible binary and ternary compounds existing in the samples. As shown in Fig.2b, the two sharp peaks at 172 and 195 $cm^{-1}$, and a weak peak at 235 $cm^{-1}$ correspond to CZTSe (Cao et al., 2012). The shoulder peak at 245 $cm^{-1}$ belonging to $MoSe_2$ that formed at the back contact has low density when measured from the top of dense and homogeneous

films (Luckert et al., 2011). Additionally, for the CZTSSe OLA sample, a wide peak at 328 $cm^{-1}$ can be attributed to the A1 mode of residual CZTS (Qu et al., 2016*a*). This peak is negligible for CZTSSe FA sample as only 2% S remains in this sample after the selenisation process. Although derived from different solvent systems, both CZTSSe thin films have a high quality kesterite crystal structure with no obvious secondary phases observed.

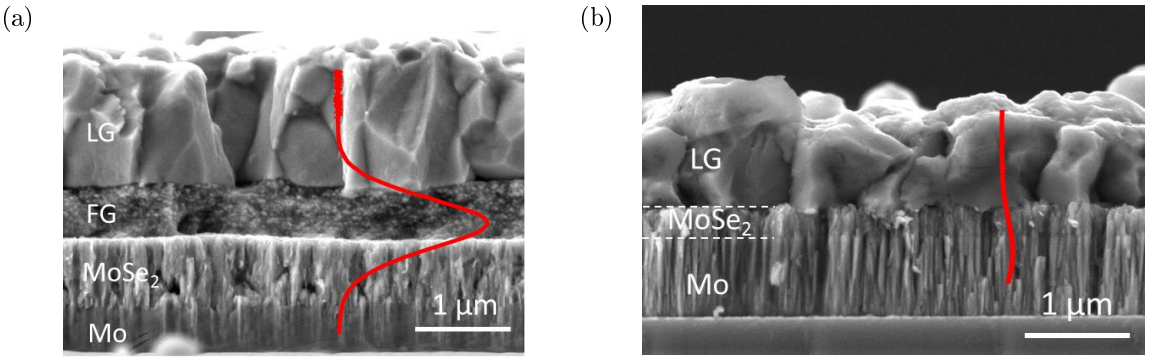


Figure 3: Cross-sectional SEM images of selenised absorber made from (a) CZTS OLA and (b) CZTS FA nanoparticle films. The depth profiles of carbon measured by GDOES across the absorbers are given as the red curve in the figures, which are a qualitative indicator of the carbon-rich FG layer.

Further to the crystal property study above, the cross-sectional morphology of thin films after selenisation are given in Fig.3. The CZTSSe OLA thin film, shown in Fig.3*a* reveals a four-layer structure. The bottom layer is the columnar grain structured Mo with $MoSe_2$ layer on top formed under the selenium-rich annealing conditions. Above the substrate, the CZTSSe absorber is composed of a bilayer structure with a top layer consisting of densely packed large grains (LG) and a bottom layer composed of fine grains (FG). In CZTSSe FA thin film however, the absorber is only composed of a

single LG CZTSSe layer as shown in *Fig.3b* in agreement with (Huang et al., 2016). Fig.3 also shows the relative carbon depth profiles in both absorber. CZTSSe OLA shows the characteristic high concentration of carbon in the FG layer while CZTSSe FA present a uniform signal throughout the absorber.

### *4.2. Excitation-dependent PL*

The power-dependent PL spectra of the OLA and FA samples, measured at 6 K under equivalent experimental conditions, are presented in Fig.4. The luminescence for both samples is dominated by a broad asymmetric band with peak energies of ∼0.91 (∼0.86) eV for OLA (FA) samples. The lower peak energy value of the FA sample could be attributed to the higher Se content, see Supp.Table 1. From the figure, the saturation of the PL peak is evident as all the defect states become populated with increasing excitation intensity.

The blue-shifting PL peak together with the emergence of a higher-energy shoulder at higher excitation intensity observed in both OLA and FA samples are indicative of QDAP defects as the dominant recombination mechanism. The significant shift to lower energy of the PL peak compared to the energy bandgap ($E_g$) of the absorber and broad asymmetric PL spectra also suggest the presence of charged defect clusters forming band tails, which consequently induce electrostatic potential fluctuations in the conduction and valence bands of the material.

The emergence of a higher-energy shoulder upon saturation of the PL peak is a further indicator that the lower-energy luminescence does not involve the bands. When the QDAP defects contributing to the PL peak saturate, further excitation injects carriers into extended band-type states

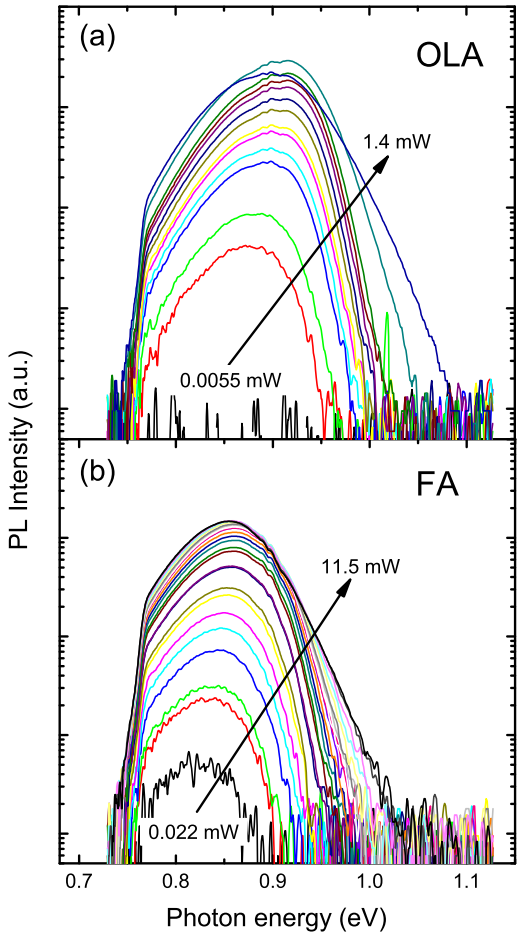


Figure 4: Excitation intensity dependencies of PL spectra in sample OLA (a) and sample FA (b) measured at 6 K.

and radiative recombination involves band-impurity or band-tail emission. A higher-energy shoulder was observed in both samples at excitation intensity exceeding the saturation threshold.

A power relationship $I \sim P^k$ was suggested (Schmidt et al., 1992) as a means of determining whether recombination is band-to-band BB ($k > 1$) or

involves defect states ($k < 1$), as previously discussed.The $k$ power coefficient is evaluated by measuring the gradient of log-log plots of $I(P)$ as shown in Fig.5. For OLA sample, the estimated value of $k$ is $0.75 \pm 0.02$. However, the plot for the FA sample suggests two linear regions which can be fitted by the power relation, with estimated $k$ values of $1.23 \pm 0.06$ and $0.70 \pm 0.02$. It should be noted that $k > 1$, while suggesting BB transitions, is not a general behaviour and it has been shown values $k > 1$ can also be observed for defect-related transitions involving neutral donors in CZTSSe absorbers (Levcenko et al., 2016). Nonetheless, it appears that several defect-related recombination mechanisms are present in the FA sample.

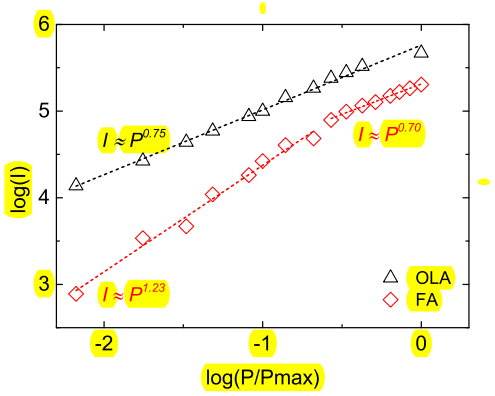


Figure 5: Log plot of the integrated PL intensity $I$ as a function of excitation power for sample OLA and FA at 6 K.

The shape $I(h\nu)$ of the PL spectra were fitted with the emperical double sigmoidal function proposed in (Krustok et al., 1999; Yakushev et al., 2017), see Supp.Fig.3. Thus, the blue-shift magnitude $\Delta E$ can be derived and QDAP separation $s$ is derived from

$$\Delta E = \frac{e^2}{4\pi\epsilon_0\epsilon_r s} \tag{5}$$

and substituting for $s$ in Eq.(4) yields QDAP density $N_D$. The calculated and experimental values of the dielectric constant and effective mass for CZTSSe from previous reports were used (Persson, 2010; Gunawan et al., 2012). The fit of the low energy tail of emissions described by Eq.(2) yields the average amplitude of electrostatic potential fluctuations $\gamma$ and the total defect density $N_t$ can be derived using Eq.(1). It should be noted that oscillations in the PL signal around 0.9 eV are due to water vapour absorption.

The optical parameters of OLA and FA absorbers are summarised in Table 1. Both samples show evidence of the presence of a fluctuating electrostatic potential with similar average amplitude $\gamma$ and are comparable to those observed in hydrazine-based CZTSSe samples studied in (Gokmen et al., 2013). The QDAP density in sample FA ($\sim 10^{16}$ cm$^{-3}$) is several orders of magnitude less than the OLA samples ($\sim 10^{18}$ cm$^{-3}$), whereas $N_t$ in all samples is similar ($\sim 10^{19}$ cm$^{-3}$). The smaller proportion of QDAP defects to total defects in sample FA suggests a larger number of non-radiative defects are present in the sample. The QDAP defect clusters also have a greater spatial separation in sample FA. In the fluctuating electrostatic potential model, electrons and holes are spatially separated and localised in potential wells within the valence and conduction bands as in Fig.1. In that case, any likely radiative recombination process requires the tunneling of charge carriers, thus an increase in the separation distance of the charged defect centres lowers the probability of a radiative transition.

| | OLA | FA |
|---|---|---|
| $E_{PL}$ (meV) | 0.907 | 0.861 |
| $\Delta E$ (meV) | 29.6 | 19.0 |
| $k$ | 0.75 | (1) 1.23 |
| | | (2) 0.70 |
| $\gamma$ (meV) | 57.5 | 51.2 |
| $E_a$ (meV) | (1) $60.3 \pm 8.2$ | $39.3 \pm 3.3$ |
| | (2) $7.6 \pm 0.6$ | |
| $E_0$ (meV) | 0.923 | 0.873 |
| Defect spacing $s$ (nm) | 6.05 | 15.87 |
| QDAP density $N_D$ ($cm^{-3}$) | 1.08 x $10^{18}$ | 5.97 x $10^{16}$ |
| Defect density $N_t$ ($cm^{-3}$) | 9.34 x $10^{19}$ | 6.98 x $10^{19}$ |

Table 1: List of optical parameters of samples OLA and FA.

### *4.3. Temperature-dependent PL*

Temperature-dependent PL was measured using a laser power just below the power at which $E_{PL}$ saturates for each sample, meaning the PL emission likely stems from pure QDAP recombination.

Fig.6 shows the PL spectra of the OLA and FA samples as a function of temperature for a fixed laser power. At 6 K, the spectrum is dominated by a peak at ∼0.91 (∼0.86) eV for the OLA (FA) sample. For the OLA sample,

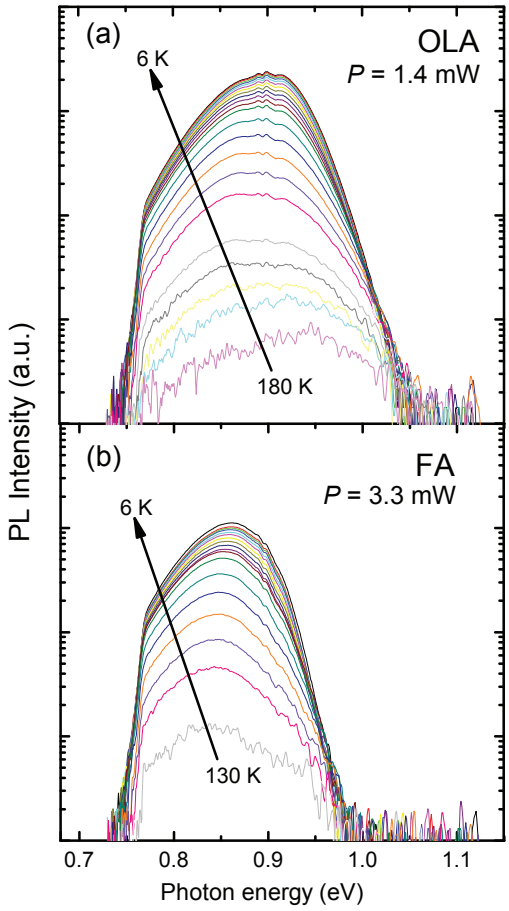


Figure 6: Temperature-dependent PL of sample OLA and FA with laser power below peak saturation intensity to avoid band-related recombination.

increasing the temperature causes this peak to red-shift up to approximately 100 K before blue-shifting. This behaviour has also been observed by Dirnstorfer et al. in $CuInGaSe_2$ (CIGSe) (Dirnstorfer et al., 1998) and by Lin et al. in CZTSSe (Lin et al., 2015). The behaviour can be explained by assuming carriers are trapped in different potential wells due to a lack of complete

thermalisation, leading to an incomplete filling of the least energetic wells. Upon increasing temperature, the carriers become more dynamic and populate the deepest wells leading to a red-shift of $E_{PL}$. When all carriers occupy deeper potentials, $E_{PL}$ reaches a minimum at the characteristic temperature of T=100 K for sample OLA. If the temperature is increased beyond the characteristic temperature, there is a blue-shift in $E_{PL}$, as shown in Fig.7a.

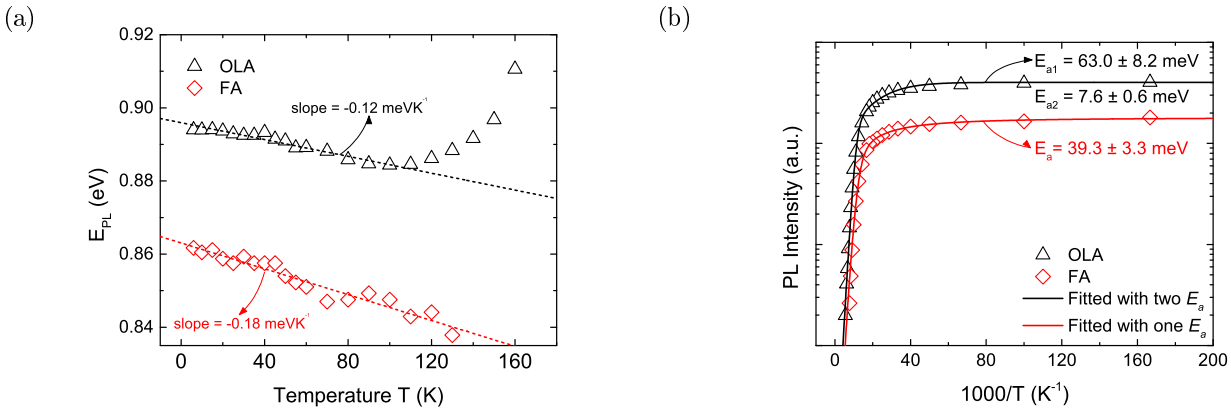


Figure 7: (a) Evolution of PL peak positions with increasing temperature $T$ for sample OLA and FA, and (b) Arrhenius plot of the integrated intensities of the PL spectra of sample OLA and FA. A two-defect model was used to fit the experimental data for sample OLA whereas a one-defect model was used to fit the sample FA data.

The more distant carrier pairs are increasingly transferred to the bands leaving the close pairs thus producing a blue-shift in the emission peak. This red-shift to blue-shift behaviour in $E_{PL}$ is indicative of the competition between QDAP transitions and band-impurity (BI) transitions with increasing temperature (Toginho Filho et al., 2005). Also it was observed that temperature dependence of $E_{PL}$ is different for both types of recombination (Bacewicz et al., 2003), where a red-shift suggests QDAP recombination and a blue-shift

indicates BI transitions. This is in agreement with the results of this study. Sample FA only exhibits a red-shift in $E_{PL}$ before the emission is quenched $\sim$ 140 K, indicating that QDAP recombination is the only radiative mechanism. A schematic of the proposed recombination mechanisms for both types of absorber is illustrated in Fig. 8.

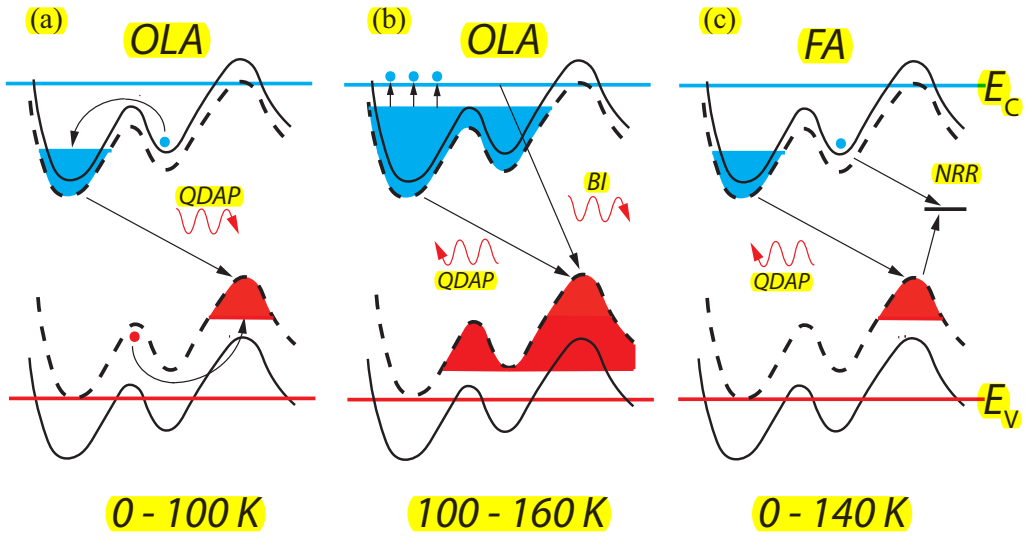


Figure 8: Schematic of proposed recombination mechanisms in OLA and FA absorbers (a) at low temperature, carriers are trapped in different potential wells and least energetic wells are not completely filled. As temperature increases, carriers become more mobile and populate the deeper wells causing a red-shift in $E_{PL}$ of QDAP transition in both absorbers, (b) above the characteristic temperature (100 K) in OLA absorber, the potential wells are filled and carriers are thermalised to the bands and radiative recombination occurs via BI transitions with a blue-shift in $E_{PL}$ (c) in FA absorber, there are a higher proportion of non-radiative defect levels and non-radiative recombination (NRR) is more prevalent, preventing the deeper wells from being completely filled.

To determine the activation energy of the defects involved in the recombination process, a one activation energy model was proposed (Krustok et al.,

1997) in the form:

$$I(T) = \frac{I_0}{1 + C_1 T^{\frac{3}{2}} + C_2 T^{\frac{3}{2}} exp\left(-\frac{E_a}{kT}\right)} \tag{6}$$

where $I_0$ is the integrated intensity extrapolated to T= 0 K, $k$ is the Boltzmann constant, $C_1$ and $C_2$ are the process rate parameters and $E_a$ are the thermal activation energies for the involved defect states. Eq.(6) was used to fit the Arrhenius plots of both samples, the fitted curve for sample FA is shown in Fig.7b. The one activation energy model provides a good fit to the experimental data for sample FA. However, the fitted curve is not accurate in the higher temperature regime of the Arrhenius plot for sample OLA. Therefore, a two activation energy model in the form of Eq.(7) (Luckert et al., 2011) was used to fit the experimental data:

$$I(T) = \frac{I_0}{1 + C_1 exp\left(-\frac{E_{a1}}{kT}\right) + C_2 exp\left(-\frac{E_{a2}}{kT}\right)} \tag{7}$$

Here $E_{a1}$ is the first activation energy, which is dominant for the high temperature region (T>100 K for sample OLA) and $E_{a2}$ is the second activation energy, which is dominant for the low temperature region (T<100 K for sample OLA).

By applying the above models values for activation energies of $E_{a1}$=63.0± 8.2 meV, $E_{a2}$=7.6 ± 0.6 meV and $E_a$=39.3 ± 3.3 meV were determined for sample OLA and FA, respectively. These values are in reasonable agreement with those reported in (Oueslati et al., 2015) where $Cu_2ZnSnSe_4$ thin films were studied. The authors proposed a recombination model with an acceptor level above the valence band and a shallow donor level below the conduction

band with an electrostatic potential fluctuation in the valence and conduction bands of the semiconductor.

For sample OLA at temperatures above the characteristic temperature the shallow donor is ionised and the transition changes from QDAP to BI transition. The BI recombination involves electrons in the conduction band and distorted acceptor levels above the valence band. Conversely, sample FA did not exhibit this change in recombination mechanism and confirms QDAP transitions are the dominant recombination process. By considering the activation energy of the defect levels in the OLA and FA absorbers in conjunction with the kesterite defect study by Chen et al., it is speculated that a defect complex ($[V_{Cu}^{-} + Zn_{Cu}^{+}]$ or $[Zn_{Sn}^{2-} + 2Zn_{Cu}^{+}]$) is present in sample OLA while a shallow acceptor antisite defect ($V_{Cu}$ or $Cu_{Zn}$) is present in sample FA (Chen et al., 2013).

### *4.4. Device fabrication and analysis*

FA and OLA CZTSSe absorbers were made into complete device structures as described earlier. While OLA-based device performed reasonably well (see later analysis) it was not possible to fabricate working solar cells using FA CZTSSe. Although Fig.3b showed a uniform FG layer-free absorber, large pores and voids are still present in the films even after a double selenisation process to densify the films (as shown in Supp.Fig.2). As a result, any device made using FA CZTSSe resulted in shunted diode with no power output. In an effort to remove the FG layer from the interface with the back contact in a working device a dual layer structure was prepared: a FA CZTS precursor was selenised to provide a carbon poor back contact

interface while OLA CZTSSe was used on top to provide a compact, void-free absorber. This results in the FG layer being sandwiched between two LG layers.

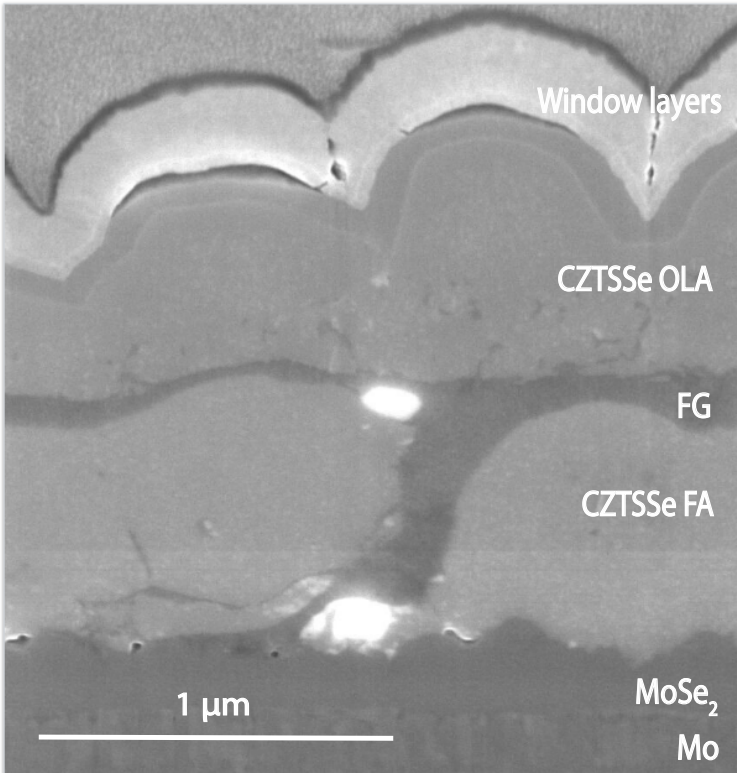


Figure 9: Cross-sectional SEM image of the device with a dual layer structure. Focused ion-beam was used to prepare this specimen. The bright areas in the FG layer are indicative of a secondary phase identified as ZnSe from EDS.

Furthermore, any voids between the CZTSSe FA grains are filled with the FG CZTSSe OLA material to ensure a continuous film as shown in Fig.9. The distribution of cell parameters of all devices across the substrate are shown in Fig.10. For both types of device, open circuit voltages ($V_{oc}$) and fill factor ($FF$) variations are uniform across each substrate.

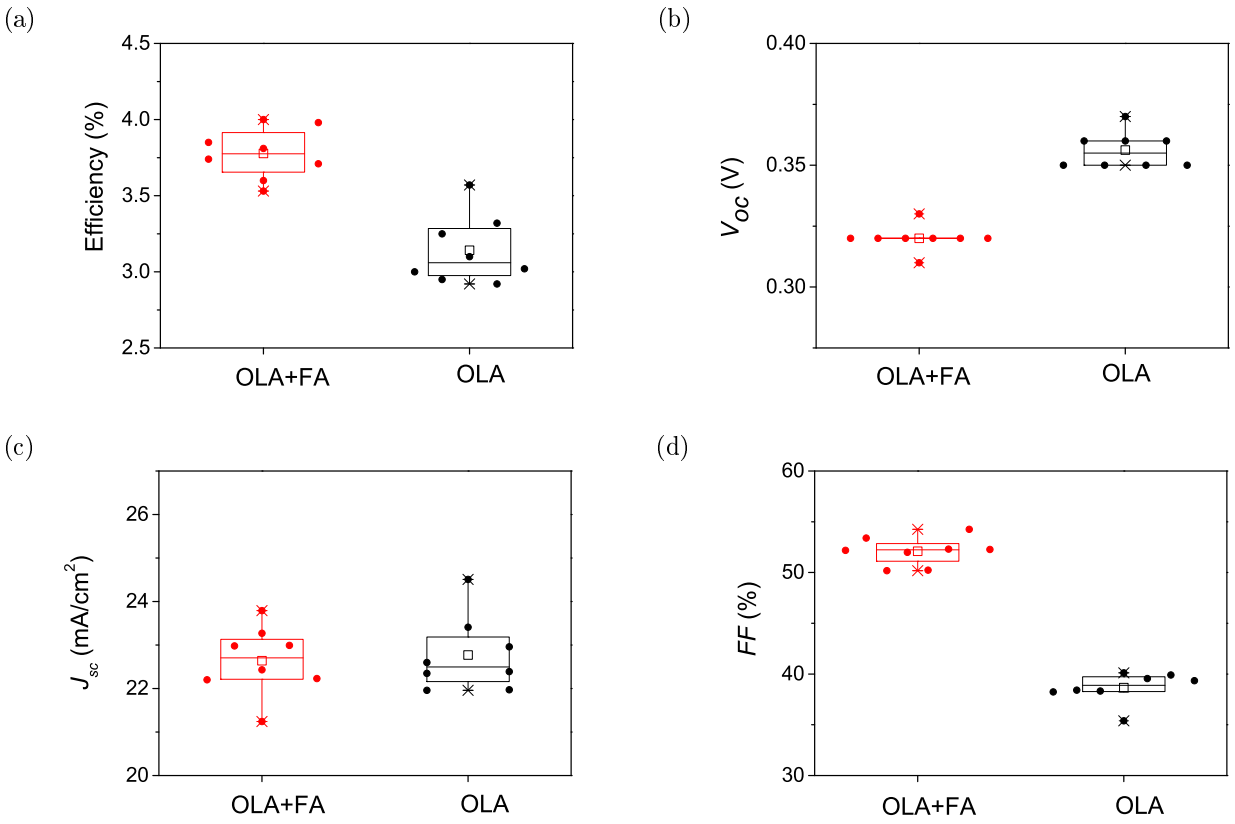


Figure 10: Box plots of the distribution of (a) efficiency, (b) $V_{oc}$, (c) $J_{sc}$ and (d) $FF$ of all devices on each substrate.

The OLA devices showed greater $V_{oc}$ (40 mV on average) compared to OLA+FA while $FF$ was significantly lower (13%). Typical illuminated series resistance ($R_{s,L}$) for an OLA cell was 2.9 $\Omega$cm$^2$ compared to a lower value of 0.6 $\Omega$cm$^2$ for an OLA+FA cell with illuminated shunt resistance ($R_{sh,L}$) values of 175 and 122 $\Omega$cm$^2$ for OLA and OLA+FA cells, respectively. The short circuit current density ($J_{SC}$) values were similar across both type of devices resulting in OLA+FA based devices outperforming those made from OLA

only absorber. The light and dark $J$-$V$ curves together with parameters of the best performing devices from each type of absorber are shown in Fig.11a and Table 2.

In-depth analysis of the most efficient OLA+FA device showed reduced series resistance ($R_{s,D}$ = 3.8 $\Omega$cm$^2$) compared with the OLA only device ($R_{s,D}$ = 7.3 $\Omega$cm$^2$). The temperature dependence of the dark series resistance ($R_{s,D}$) was studied. Using a standard diode analysis of a thin-film solar cell (Sites and Mauk, 1989; Hegedus and Shafarman, 2004), $R_s$ is extracted from the $y$ intercept of the $dV/dJ$ versus $1/(J+J_L)$ plot according to

| CZTSSe cell | $\eta$ (%) | $FF$ (%) | $V_{OC}$ (V) | $J_{SC}$ (mA/cm$^2$) | $R_{s,L}$ ($\Omega$ cm$^2$) | $R_{sh,L}$ ($\Omega$ cm$^2$) | $n$ | $J_0$ (mA/cm$^2$) |
|---|---|---|---|---|---|---|---|---|
| OLA | 3.6 | 39.4 | 0.37 | 24.5 | 2.86 | 175 | 4.01 | 4.82 x $10^{-1}$ |
| OLA+FA | 4.0 | 54.3 | 0.32 | 23.8 | 0.57 | 122 | 1.96 | 2.75 x $10^{-2}$ |

Table 2: Device parameters for the CZTSSe cells at room temperature. $R_{s,L}$, $R_{sh,L}$, $n$ and $J_0$ are the series resistance, shunt resistance, ideality factor and reverse saturation current respectively, measured using the light $J$-$V$ data. All parameters were determined using methods described in (Hegedus and Shafarman, 2004).

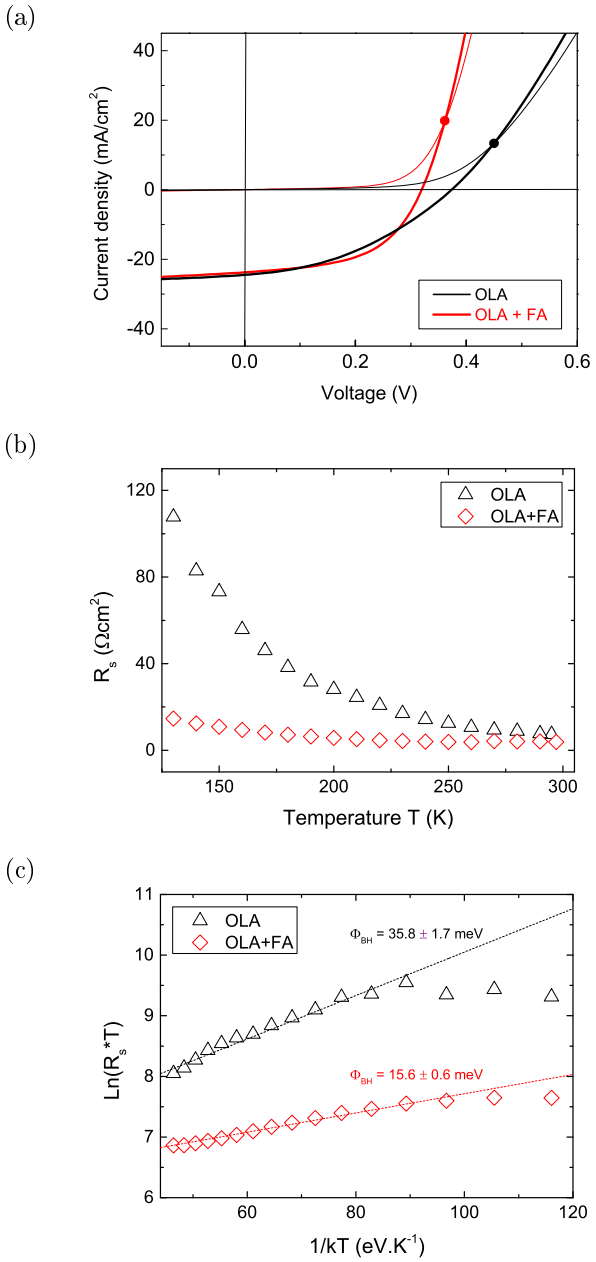


Figure 11: (a) Light (thick curves) and dark (thin curves) $J$-$V$ charactersitics of OLA and OLA+FA CZTSSe solar cells. Solid circles mark the cross-over point between light and dark $J$-$V$ curves, (b) temperature-dependent dark series resistance and (c) barrier height extraction from $\ln(R_s T)$ vs $1/T$ plot, the dashed line is the fit to Eq.(9).

$$\frac{dV}{dJ} = R_s + \frac{nkT}{q(J + J_L)} \tag{8}$$

where *n, k, T, q and* $J_L$ are the diode ideality factor, Boltzmann constant, temperature, electron charge and photogenerated current density, respectively. Dark (as opposed to illuminated) series resistance was chosen to avoid any light-induced fluctuations in the series resistance that may occur under illumination. In this case, $J_L$=$J_{SC}$=0.

Fig.11b shows the diverging dark series resistance of the OLA and OLA+FA cells towards lower temperature. $R_{s,D}$ of the OLA cell increases ~17 fold from 300 to 130 K compared to only ~4 fold increase for the OLA+FA cell. An explanation for this diverging series resistance is the presence of a blocking back-contact (Schottky) barrier as proposed by (Gunawan et al., 2010). The presence of the barrier would act to suppress the hole transport across the Mo back contact to the CZTSSe absorber layer. In this Schottky diode model , the total series resistance $R_{s,D}$ in the solar cell is given by

$$R_{s,D} = R_0 + \frac{k}{qA^*T} exp\left(\frac{\Phi_{BH}}{kT}\right) \tag{9}$$

where $A^*$ is the effective Richardson constant, $\Phi_{BH}$ is the barrier height, $R_0$ is the background series resistance, due to top contact and bulk resistance which is usually small and approximately constant and therefore neglected in this analysis. From *ln($R_sT$)* versus *1/kT* plot, Eq.(9) is fitted to the high temperature region (low *1/kT*) of the curve and the slope yields a barrier height $\Phi_{BH}$ of 15.6 and 35.8 meV for the OLA+FA and OLA cells, respectively (see Fig.11c). The low barrier height for the OLA+FA device

could be considered a quasi-ohmic contact, as evidenced by lower $R_{s,D}$ and higher $FF$ compared to the OLA device. A similar trend in device parameters was reported by Gunawan et al. (2010).

Both devices showed crossover of the dark and light $J$-$V$ curves, as indicated by the solid circles in Fig.11a. These crossover points occur at a lower current value for the OLA cell than the OLA+FA cell also demonstrating the presence of a larger barrier in the OLA device (McCandless et al., 1998). An alternate explanation for the observed divergence of $R_{s,D}$ has been hypothesised. Admittance spectroscopy analysis of CZTSSe solar cells by (Gunawan et al., 2012) showed the apparent divergent behaviour in $R_{s,D}$ arises out of a carrier freeze-out effect due to lack of shallow acceptors in the CZTSSe absorbers.

The temperature dependence of $n$ for both devices are shown in Fig.12a. It is evident that the ideality factor for both types of device increases above two as temperature reduces, suggesting a mechanism other than Shockley-Read-Hall (SRH) recombination is present. Regarding SRH recombination, $n$ assumes values between one and two and is almost independent of temperature. A number of factors influence the value of $n$, such as recombination centre(s) energy, their capture cross-section, distribution and location within the absorber. (Hegedus and Shafarman, 2004; Rau, 1999; Walter et al., 1996; Courel et al., 2017).

One explanation for the temperature dependent behaviour of $n$ arises from a tunneling-enhanced recombination mechanism, where the SRH recombination rate is augmented by contributions from tunneling (Rau, 1999; Nadenau et al., 2000; Hurkx et al., 1992). Tunneling enhanced recombina-

tion can occur (i) in the depletion region of the *pn*-junction due to high densities of mid-gap defect states (*bulk*-dominated tunneling-enhanced recombination) and (ii) at the heterojunction between absorber and buffer due to high densities of interface defect states (*interface*-dominated tunneling-enhanced recombination). Such a tunneling-enhanced recombination model is frequently applied to Cu(In,Ga)(S,Se)$_2$ (CIGSSe) and CdTe based solar cells (Courel et al., 2017) where the tunneling-enhanced recombination current is found to increase with increasing characteristic tunneling energy ($E_{00}$) and decreasing temperature. Application of this model reveals a continuous transition of $n$ to values greater than two as the temperature is decreased, similar to the ideality factor data for the CZTSSe devices presented here.

In considering *bulk*-dominated tunneling-enhanced recombination mechanism, the ideality factor can be expressed as

$$\frac{1}{n} = \frac{1}{2}\left(1 - \frac{E_{00}^2}{3(kT)^2} + \frac{T}{T^*}\right) \tag{10}$$

where $E_{00}$ is the characteristic tunneling energy and $kT^*$ is the characteristic energy of the distribution of trap states near the band edge associated with band-tailing or potential fluctuations (Hages et al., 2014). Fitting Eq.(10) to $1/n$ versus $T$ plots in Fig.12b yields an estimate of $E_{00}$ values of 19.3 and 19.8 meV for sample OLA and OLA+FA respectively, comparable to values determined by Hages et al. (Hages et al., 2014). Nadenau et al. showed a close relationship between open-circuit voltage $V_{oc}$ and the characteristic tunneling energy $E_{00}$, where a link was established between efficiency gain in use of Ga-rich CuGaSe$_2$ absorbers and decreased tunneling rates. They suggest device modifications such as the change of CdS deposition tempera-

ture have beneficial effects of lowered $E_{00}$ and increased $V_{oc}$ (Nadenau et al., 2000).

It is apparent that a tunneling enhanced mechanism dominates in both devices at low temperature with a reducing tunneling contribution as $T$ approaches 300 K. The possibility of *interface*-dominated tunneling-enhanced recombination was considered but discounted following analysis of the experimental data, further details of which can be found in supplementary information section.

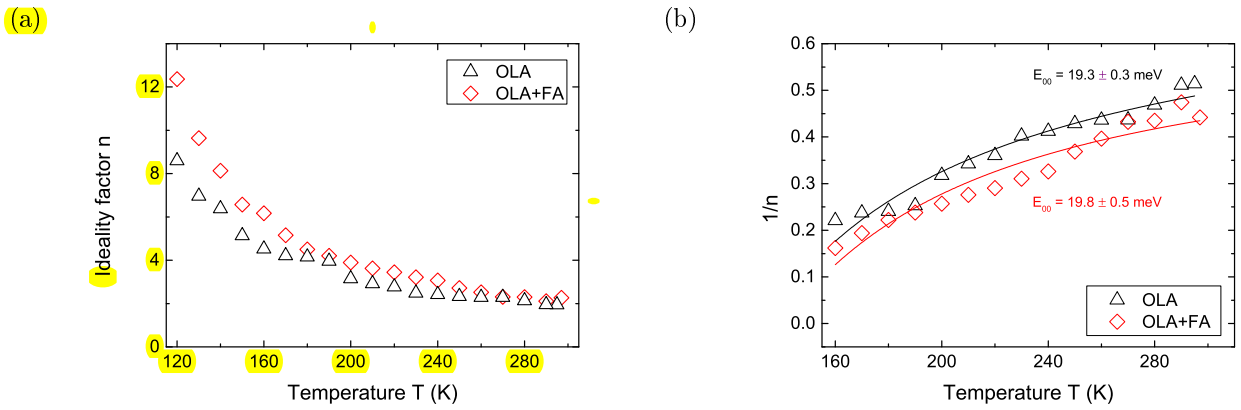


Figure 12: (a) Temperature-dependent ideality factor $n$ and (b) $1/n(T)$ vs $T$ plot. The solid fitted lines to the data represent a fit to Eq.(10) for the measured data.

## 5. Conclusion

The luminescence properties of CZTSSe thin film layers prepared from CZTS nanoparticle inks have been investigated with respect to the ligand type used during the nanocrystal synthesis.It is suspected that QDAP is the dominating recombination mechanism in both type of absorbers showing

similar level of potential fluctuation ($\sim$50 meV). The temperature dependent PL analysis revealed a shift in recombination mechanism in OLA CZTSSe from QDAP to BI as temperature increases while QDAP remained the sole recombination process in FA CZTSSe. Due to the porosity of the FA CZTSSe layer it was not possible to produce solar device however when using a dual layer FA+OLA this was found to outperform devices based on OLA CZTSSe alone. The main reason for this was the reduction of the back contact barrier height in FA+OLA devices yielding lower series resistance and higher fill factor. This is a consequence of the removal of the fine grain layer at the Mo back contact interface and gives promising new outlook for this particular synthesis route.

## 6. Acknowledgments

The authors acknowledge support from the Engineering and Physical Sciences Research Council (EPSRC) via Grants EP/N024389/1 and EP/R021503/1 and the North East Centre for Energy Materials (NECEM). The assistance with Raman spectroscopy by Dr. Kate Nicholson, Department of Applied Sciences, Northumbria University is also acknowledged.

## 7. References


Bacewicz, R., Żuk, P. and Trykozko, R. (2003), 'Photoluminescence study of ZnO/CdS/Cu(In,Ga)$Se_2$ solar cells', *Opto - Electronics Review* **Vol. 11, No. 4**, 277–280.

Bourdais, S., Choné, C., Delatouche, B., Jacob, A., Larramona, G., Moisan, C., Lafond, A., Donatini, F., Rey, G. and Siebentritt, S. (2016), 'Is the Cu/Zn Disorder the Main Culprit for the Voltage Deficit in Kesterite Solar Cells?', *Advanced Energy Materials* **6**(12), 1502276.

Cao, Y., Denny, M. S., Caspar, J. V., Farneth, W. E., Guo, Q., Ionkin, A. S., Johnson, L. K., Lu, M., Malajovich, I. and Radu, D. (2012), 'High-Efficiency Solution-Processed $Cu_2ZnSn(S,Se)_4$ Thin-Film Solar Cells Prepared from Binary and Ternary Nanoparticles', *Journal of the American Chemical Society* **134**(38), 15644–15647.
**URL:** *http://dx.doi.org/10.1021/ja3057985*

Chen, S., Walsh, A., Gong, X.-G. and Wei, S.-H. (2013), 'Classification of Lattice Defects in the Kesterite $Cu_2ZnSnS_4$ and $Cu_2ZnSnSe_4$ Earth-Abundant Solar Cell Absorbers', *Advanced Materials* **25**(11), 1522–1539.

Courel, M., Valencia-Resendiz, E., Andrade-Arvizu, J., Saucedo, E. and Vigil-Galán, O. (2017), 'Towards understanding poor performances in spray-deposited $Cu_2ZnSnS_4$ thin film solar cells', *Solar Energy Materials and Solar Cells* **159**, 151–158.

Dirnstorfer, I., Wagner, M., Hofmann, D., Lampert, M., Karg, F. and Meyer,

B. (1998), 'Characterization of CuIn(Ga)$Se_2$ thin films', *Physica Status Solidi (a)* **168**(1), 163–175.

Gershon, T., Shin, B., Bojarczuk, N., Gokmen, T., Lu, S. and Guha, S. (2013), 'Photoluminescence characterization of a high-efficiency $Cu_2ZnSnS_4$ device', *Journal of Applied Physics* **114**(15), 154905.
**URL:** *http://dx.doi.org/10.1063/1.4825317*

Gokmen, T., Gunawan, O., Todorov, T. K. and Mitzi, D. B. (2013), 'Band tailing and efficiency limitation in kesterite solar cells', *Applied Physics Letters* **103**(10), 103506.
**URL:** *http://dx.doi.org/10.1063/1.4820250*

Gunawan, O., Gokmen, T., Warren, C. W., Cohen, J. D., Todorov, T. K., Barkhouse, D. A. R., Bag, S., Tang, J., Shin, B. and Mitzi, D. B. (2012), 'Electronic properties of the $Cu_2ZnSn(Se,S)_4$ absorber layer in solar cells as revealed by admittance spectroscopy and related methods', *Applied Physics Letters* **100**(25), 253905.
**URL:** *http://dx.doi.org/10.1063/1.4729751*

Gunawan, O., Todorov, T. K. and Mitzi, D. B. (2010), 'Loss mechanisms in hydrazine-processed $Cu_2ZnSn(Se,S)_4$ solar cells', *Applied Physics Letters* **97**(23), 233506.
**URL:** *http://dx.doi.org/10.1063/1.3522884*

Hages, C. J., Carter, N. J., Agrawal, R. and Unold, T. (2014), 'Generalized current-voltage analysis and efficiency limitations in non-ideal solar cells: Case of $Cu_2ZnSn(S_xSe_{1-x})_4$ and $Cu_2Zn(Sn_yGe_{1-y})(S_xSe_{1-x})_4$', *Journal of*

*Applied Physics* **115**(23), 234504.
**URL:** *http://dx.doi.org/10.1063/1.4882119*

Hages, C. J., Carter, N. J., Moore, J., McLeod, S. M., Miskin, C. K., Joglekar, C., Lundstrom, M. S. and Agrawal, R. (2013), Device comparison of champion nanocrystal-ink based CZTSSe and CIGSSe solar cells: Capacitance spectroscopy, *in* '2013 IEEE 39th Photovoltaic Specialists Conference (PVSC)', pp. 1966–1971.

Hages, C. J., Koeper, M. J., Miskin, C. K., Brew, K. W. and Agrawal, R. (2016), 'Controlled Grain Growth for High Performance Nanoparticle-Based Kesterite Solar Cells', *Chemistry of Materials* **28**(21), 7703–7714.
**URL:** *http://dx.doi.org/10.1021/acs.chemmater.6b02733*

Hegedus, S. S. and Shafarman, W. N. (2004), 'Thin-film solar cells: device measurements and analysis', *Progress in Photovoltaics: Research and Applications* **12**(23), 155–176.

Huang, T. J., Yin, X., Tang, C., Qi, G. and Gong, H. (2015), 'A low-cost, ligand exchange-free strategy to synthesize large-grained $Cu_2ZnSnS_4$ thin-films without a fine-grain underlayer from nanocrystals', *J. Mater. Chem. A* **3**(34), 17788–17796.
**URL:** *http://dx.doi.org/10.1039/C5TA03640B*

Huang, T. J., Yin, X., Tang, C., Qi, G. and Gong, H. (2016), 'Influence of Ligands on the Formation of Kesterite Thin Films for Solar Cells: A Comparative Study', *ChemSusChem* **9**(9), 1032–1041.
**URL:** *http://dx.doi.org/10.1002/cssc.201600063*

Hurkx, G., Klaassen, D. and Knuvers, M. (1992), 'A new recombination model for device simulation including tunneling', *IEEE Transactions on Electron Devices* **39**(2), 331–338.
**URL:** *http://10.1109/16.121690*

Krustok, J., Collan, H. and Hjelt, K. (1997), 'Does the low-temperature Arrhenius plot of the photoluminescence intensity in CdTe point towards an erroneous activation energy?', *Journal of Applied Physics* **81**(3), 1442–1445.

Krustok, J., Collan, H., Yakushev, M. and Hjelt, K. (1999), 'The role of spatial potential fluctuations in the shape of the PL bands of multinary semiconductor compounds', *Physica Scripta* **T79**(1), 179.

Levanyuk, A. P. and Osipov, V. V. (1981), 'Edge luminescence of direct-gap semiconductors', *Soviet Physics Uspekhi* **24**(3), 187–215.

Levcenko, S., Just, J., Redinger, A., Larramona, G., Bourdais, S., Dennler, G., Jacob, A. and Unold, T. (2016), 'Deep defects in$Cu_2ZnSn(S,Se)_4$ Solar Cells with Varying Se Content', *Physical Review Applied* **5**(2).

Lin, X., Ennaoui, A., Levcenko, S., Dittrich, T., Kavalakkatt, J., Kretzschmar, S., Unold, T. and Lux-Steiner, M. C. (2015), 'Defect study of $Cu_2ZnSn(S_xSe_{1-x})_4$ thin film absorbers using photoluminescence and modulated surface photovoltage spectroscopy', *Applied Physics Letters* **106**(1), 013903.

Luckert, F., Hamilton, D. I., Yakushev, M. V., Beattie, N. S., Zoppi, G., Moynihan, M., Forbes, I., Karotki, A. V., Mudryi, A. V. and Grossberg, M.

(2011), 'Optical properties of high quality $Cu_2ZnSnSe_4$ thin films', *Applied Physics Letters* **99**(6), 062104.
**URL:** *http://10.1063/1.3624827*

McCandless, B., Phillips, J. and Titus, J. (1998), *Characterizing contacts to p-type CdTe in CdS/CdTe solar cells*, pp. 448–452.

Nadenau, V., Rau, U., Jasenek, A. and Schock, H. W. (2000), 'Electronic properties of $CuGaSe_2$-based heterojunction solar cells. Part i. Transport analysis', *Journal of Applied Physics* **87**(1), 584–593.
**URL:** *http://10.1016/j.solmat.2014.10.041*

Oueslati, S., Brammertz, G., Buffière, M., Köble, C., Oualid, T., Meuris, M. and Poortmans, J. (2015), 'Photoluminescence study and observation of unusual optical transitions in $Cu_2ZnSnSe_4$/CdS/ZnO solar cells', *Solar Energy Materials and Solar Cells* **134**, 340–345.
**URL:** *http://10.1016/j.solmat.2014.10.041*

Persson, C. (2010), 'Electronic and optical properties of $Cu_2ZnSnS_4$ and $Cu_2ZnSnSe_4$', *Journal of Applied Physics* **107**(5), 053710.
**URL:** *http://dx.doi.org/10.1063/1.3318468*

Qu, Y., Zoppi, G. and Beattie, N. S. (2016*a*), 'The role of nanoparticle inks in determining the performance of solution processed $Cu_2ZnSn(S,Se)_4$ thin film solar cells', *Progress in Photovoltaics: Research and Applications* **24**(6), 836–845.
**URL:** *http://dx.doi.org/10.1002/pip.2756*

Qu, Y., Zoppi, G. and Beattie, N. S. (2016*b*), 'Selenization kinetics in $Cu_2ZnSn(S,Se)_4$ solar cells prepared from nanoparticle inks', *Solar Energy Materials and Solar Cells* **158**, 130–137.

Qu, Y., Zoppi, G., Miles, R. W. and Beattie, N. S. (2014), 'Influence of reaction conditions on the properties of solution-processed $Cu_2ZnSnS_4$ nanocrystals', *Materials Research Express* **1**(4), 045040.
**URL:** *http://dx.doi.org/10.1002/cssc.201600063*

Rau, U. (1999), 'Tunneling-enhanced recombination in $Cu(In,Ga)Se_2$ heterojunction solar cells', *Applied Physics Letters* **74**(1), 111–113.
**URL:** *http://dx.doi.org/10.1063/1.122967*

Schmidt, T., Lischka, K. and Zulehner, W. (1992), 'Excitation-power dependence of the near-band-edge photoluminescence of semiconductors', *Physical Review B* **45**(16), 8989–8994.

Schumacher, S. A., Botha, J. R. and Alberts, V. (2006), 'Photoluminescence study of potential fluctuations in thin layers of $Cu(In_{0.75}Ga_{0.25})(S_ySe_{1-y})_2$', *Journal of Applied Physics* **99**(6), 063508.
**URL:** *http://dx.doi.org/10.1063/1.2180429*

Scragg, J. J. S., Larsen, J. K., Kumar, M., Persson, C., Sendler, J., Siebentritt, S. and Platzer Bjorkman, C. (2015), 'Cu-Zn disorder and band gap fluctuations in $Cu_2ZnSn(S,Se)_4$ Theoretical and experimental investigations', *Physica Status Solidi (b)* **253**(2), 247–254.

Shklovskij, B. I. and Efros, A. L. (1984), *Electronic properties of doped semiconductors*, Springer.

Siebentritt, S., Papathanasiou, N. and Lux-Steiner, M. (2006), 'Potential fluctuations in compensated chalcopyrites', *Physica B: Condensed Matter* **376-377**, 831–833.

Sites, J. and Mauk, P. (1989), 'Diode quality factor determination for thin-film solar cells', *Solar Cells* **27**(1-4), 411–417.
**URL:** *https://doi.org/10.1016/0379-6787(89)90050-1*

Tai, K. F., Gershon, T., Gunawan, O. and Huan, C. H. A. (2015), 'Examination of electronic structure differences between CIGSSe and CZTSSe by photoluminescence study', *Journal of Applied Physics* **117**(23), 235701.
**URL:** *http://dx.doi.org/10.1063/1.4922493*

Toginho Filho, D. O., Dias, I. F. L., Laureto, E., Duarte, J. L., Lourenço, S. A., Poças, L. C., Prabhu, S. S. and Klem, J. (2005), 'Quasi-donor-acceptor pair transitions in GaAsSb and AlGaAsSb on InP', *Journal of Applied Physics* **97**(12), 123702.
**URL:** *http://dx.doi.org/10.1063/1.1923588*

Walter, T., Herberholz, R., Müller, C. and Schock, H. W. (1996), 'Defect Distribution and Metastability in Chalcopyrite Semiconductors', *MRS Proceedings* **426**.

Wang, W., Shen, H., Wong, L. H., Su, Z., Yao, H. and Li, Y. (2016), 'A 4.92% efficiency $Cu_2ZnSnS_4$ solar cell from nanoparticle ink and molecular solution', *RSC Advances* **6**(59), 54049–54053.

Yakushev, M., Sulimov, M., Márquez-Prieto, J., Forbes, I., Krustok, J., Edwards, P., Zhivulko, V., Borodavchenko, O., Mudryi, A. and Martin, R.

(2017), 'Influence of the copper content on the optical properties of CZTSe thin films', *Solar Energy Materials and Solar Cells* **168**, 69–77.

Yu, P. W. (1977), 'Excitation-dependent emission in Mg-, Be-, Cd-, and Zn-implanted GaAs', *Journal of Applied Physics* **48**(12), 5043–5051.

## AppendixA. Supplementary material

### *AppendixA.1. Equipment details*

The PL spectra were measured using a Horiba Jobin Yvon iHR320 fully automated spectrometer fitted with an InGaAs PMT detector cooled to -30°C to reduce noise. A 532 nm continuous wave diode-pumped solid state (CW-DPSS) laser (MGL III-532 200 mW) was used as an excitation source. Power-dependent PL measurements were performed by adjusting the intensity of the laser beam using the MGL PSU-III-LED controller. PL measurements at varying temperatures were performed by placing the sample in a Janis SHI-4-2 closed cycle refrigeration cryostat using compressed He gas coupled with a Lakeshore Model 335 temperature controller. The laser light was chopped and focused onto the sample inside the cryostat and luminescence from the sample was focused into the entrance slit of the 320 mm focal length monochromator, containing a grating with 900 grooves/mm. In order to avoid higher order artefacts arising from laser radiation, the luminescence was filtered with a long-pass filter with a cut-off wavelength of 760 nm. The chopped signal was detected with the themoelectrically cooled InGaAs detector and amplified with a Stanford Research Systems SR810 DSP lock-in amplifier connected to the chopper signal.

### *AppendixA.2. Nanoparticle synthesis*

CZTS OLA recipe

1.34 mmol of copper(II) acetylacetonate, 0.95 mmol of zinc acetylacetonate, 0.75 mmol of tin(IV) bis(acetylacetonate) dichloride were dissolved into 10 ml oleylamine (OLA) in a three necks flask connected to the Schlenk line.

The reaction mixture was put under vacuum and purged with nitrogen twice to remove residual water and oxygen dissolved in the solvent. After the degassing process, the temperature of the mixture was then increased to the reaction temperature of 225 °C after which 3 ml 1M sulphur-OLA solution was then injected into the solvent. The reaction solution was then held at the reaction temperature for 30 min to allow the growth of the CZTS nanoparticles. After reaction, the CZTS nanoparticles were collected and washed twice using IPA and toluene. The CZTS OLA nanoparticle ink was prepared by dispersing nanoparticles into hexanethiol with the aid of sonication.

CZTS FA recipe

Firstly, 4.8 mmol of copper(II) acetate monohydrate, 3.3 mmol of $SnCl_2$, 3.12 mmol of $ZnCl_2$ were dissolved successively into 20 ml formamide to make the metal solution in a glass bottle. Next, 13.2 mmol thioacetamide (TAA) dissovled into 10 ml formamide (FA) at room temperature in a three necks flask connected to the Schlenk line. The TAA solution was put under vacuum and purged with nitrogen twice to remove residual water and oxygen dissolved in the solvent. After the degassing process, the temperature of the mixture was then increased to the reaction temperature of 170 °C after which 2.5 ml metal solution was injected into the TAA solution. The reaction was allowed to hold for 2 min before put the reaction flask into a cold water bath to cease the reaction. After the reaction, ethanol and FA were used to precipitate and wash the CZTS nanoparticles twice before suspending nanoparticles in ethanol to yield the CZTS FA nanoparticle ink.

Spin-coating

Approximately 50 $\mu$l of the concentrated ink was applied onto a square (2.5

cm x 2.5 cm) Mo-coated glass substrate at a speed of 1200 rpm for 5 seconds. The samples were then dried on a hot plate at ∼150 (∼100) °C for 30 seconds and then at ∼300 (∼200) °C in air for 30 seconds for OLA (FA) samples to remove the residual solvents. The spin coating and soft-baking procedures were repeated 10 times to yield thin films with a thickness of ∼ 1$\mu$m.

Supplementary Table 1: The composition of precursor and selenised films on bare SLG

| Solvent | | $Cu$ ($at\%$) | $Zn$ ($at\%$) | $Sn$ ($at\%$) | $S$ ($at\%$) | $Se$ ($at\%$) | $\frac{Cu}{Zn+Sn}$ | $Zn/Sn$ | $\frac{Se}{Se+S}$ |
|---|---|---|---|---|---|---|---|---|---|
| OLA | Precursor | 24.0 | 16.2 | 14.1 | 45.7 | | 0.79 | 1.15 | |
| | Selenised | 22.4 | 12.6 | 12.7 | 5.8 | 46.6 | 0.89 | 1.00 | 0.89 |
| FA | Precursor | 21.8 | 16.3 | 12.8 | 49.1 | | 0.76 | 1.30 | |
| | Selenised | 19.0 | 12.2 | 11.2 | 1.9 | 55.7 | 0.81 | 1.09 | 0.98 |

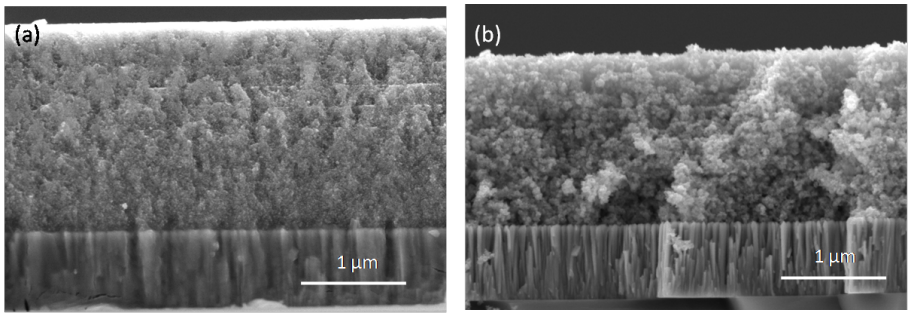


Supplementary Figure 1: Cross-sectional SEM images of precursor thin films made from (a) CZTS OLA nanoparticles and (b) CZTS FA nanoparticles.

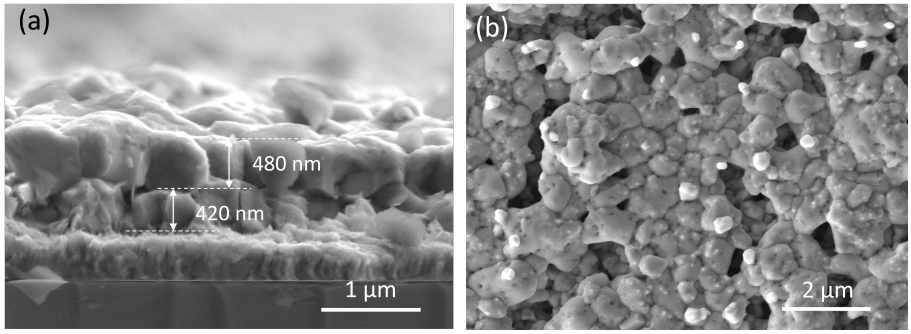


Supplementary Figure 2: Cross sectional and top view SEM images of the double selenised CZTSSe FA thin film. Five layers CZTS FA film was selenised followed by the selenisation of another five layers CZTS FA on top to attempt densifying the absorber. As shown in Figure (a), the double selenised CZTSSe FA thin film is composed of two large grain layers. However, the thin film is still highly porous as shown in Figure (b).

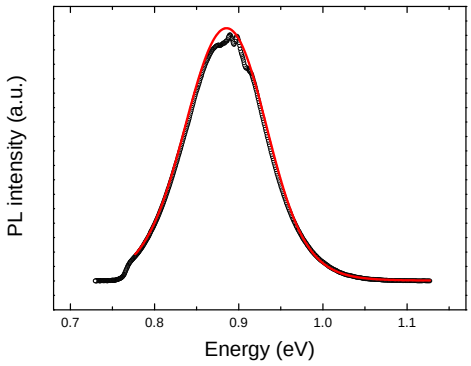


Supplementary Figure 3: The PL spectrum (circle symbols) of sample OLA measured at 6K, fitted with asymmetric double sigmoidal function (solid red line). The oscillation in the PL signal around 0.9 eV is due to water vapour absorption.

*AppendixA.3. Interface tunneling-enhanced recombination*

In the limit of *interface*-dominated tunneling-enhanced recombination mechanism, the ideality factor follows

$$n = \frac{E_{00}}{kT} coth\left(\frac{E_{00}}{kT}\right) \tag{A.1}$$

However, analysis of *n(T)* according to Eq.(A.1) did not provide a good fit for the experimental data, see Supp.Fig.4. Applying this model to the data yields $E_{00}$ values of $\approx 56$ and $\approx 64$ meV for sample OLA and OLA+FA, respectively. In order to ascertain which recombination mechanism is dominant in the OLA and OLA+FA devices, the origin of the characteristic tunnelling energy can be considered, according to (Rau, 1999)

$$E_{00} = \left(\frac{q\hbar}{2}\right)\left(\frac{N_A}{m^* \epsilon_s}\right)^{\frac{1}{2}} \tag{A.2}$$

where $\hbar$ is the reduced Planck constant, $N_A$ is the net doping density , $m^*$ is the effective tunneling mass, and $\epsilon_s$ is the dielectric constant of the semiconductor material whose values determined by (Persson, 2010; Gunawan et al., 2012) were used.

If *bulk* tunneling-enhanced recombination is assumed to be the dominant mechanism, using Eq.(A.2) results in a net doping density of $\approx 6$ x $10^{17}$ and $\approx$ 7 x $10^{17}$ cm$^{-3}$ for the OLA and OLA+FA devices, respectively. The estimate of the net doping density is reasonable under the *bulk*-dominant tunneling enhanced recombination mechanism, specifically for recombination in the space charge region (SCR) near the junction where high defect densities are to be expected (Hages et al., 2013). However, using Eq.(A.2) to evaluate the

net doping density from $E_{00}$ values assumed under the *interface*-tunneling model gives $N_A$ values of $\approx 8 \times 10^{18}$ cm$^{-3}$. This would indicate a substantially high recombination current at the CdS/CZTSSe interface and would lead to a significant reduction in $J_{SC}$. Such a reduction was not observed in either device under study. Furthermore, Hages et al. state that the *bulk* tunneling-enhanced recombination mechanism correlates with the potential fluctuations model (as discussed previously) from $J_0(T)$ analysis.

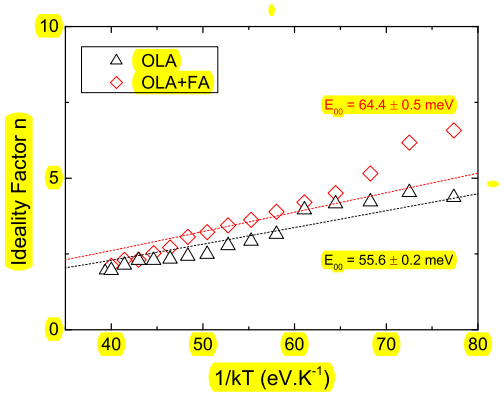


Supplementary Figure 4: $n(T)$ vs $1/kT$ plot. The dashed lines represent a fit to Eq.(A.1).